From a WGS84 Lollipop to Frame-Aware Control on $\mathbb{S}^2$

An exact holonomy response for anisotropic removal kernels

Heah Hung Xun

Department of Physics, Xiamen University Malaysia

PHY2409025@xmu.edu.my

10 September 2026

Abstract

Removing material from a spherical lollipop to reproduce the flattening of the WGS84 ellipsoid motivates a model of localized actuation on the sphere. An elongated footprint requires a tangent direction as well as a contact point. We represent this state by an oriented orthonormal frame and transport it with the Levi-Civita connection. For a compactly supported Gaussian in logarithmic coordinates, we derive an exact one-dimensional integral for the L^2 mismatch between footprints whose frames differ by an angle ψ. The formula characterizes all zero-response angles, gives the leading response to weak anisotropy, and converts enclosed spherical area into a quantitative change in actuation. A one-contact approximation problem has strictly positive error whenever its available orientation differs from the target modulo π. For finite non-negative dictionaries we establish existence and uniqueness of the fitted field and evaluate a nested-orientation benchmark. Independent polar quadrature checks the overlap formula, and step refinement verifies fourth-order convergence of numerical parallel transport. The lollipop target occupies only degrees zero and two at first order in flattening. The results concern a fixed reference sphere and additive removal; they do not require a model of evolving-surface mechanics.

1 From total mass loss to an oriented contact

This work began by thinking about a lollipop: how should one lick a sphere so that its final shape has the flattening of the WGS84 reference ellipsoid? A volume calculation determines how much material to remove but does not determine where to remove it. Uniform removal preserves spherical symmetry. Flattening instead requires greater radial reduction near the poles than near the equator. An elongated contact introduces a second question: which direction should that contact point?

Let $\delta_\star : \mathbb{S}^2 \to \mathbb{R}_{\geq 0}$ describe a desired small radial removal on a fixed reference sphere. The accumulated field is

$$\delta_N(y) = \sum_{j=1}^{N} \alpha_j K(y; R_j), \qquad \alpha_j \geq 0. \tag{1}$$

Each kernel has unit integral, so α_j is the integral of radial removal over solid angle. On a physical sphere of radius R_0, the first-order removed volume is $R_0^2 \alpha_j$. A frame R_j specifies both the centre and the tangent axes. The geometry is held fixed during actuation, and removal during travel is excluded unless represented by additional contacts. These are modelling assumptions rather than a mechanical law for candy dissolution or polishing.

Directional spherical wavelets provide localized analysis with an orientation variable [2]. Gauge-equivariant convolution makes tangent frames and their changes explicit [3]; parallel-transport convolution preserves directionality on manifolds [4]. Path-dependent transported orientations are already part of this literature. In surface processing, local influence functions underpin computer-controlled polishing [5], and tool-path direction and elliptic contact affect the removal map [6].

Our main result is an explicit overlap formula for two anisotropic contacts at the same centre (Theorem 4.1). It gives the exact orientation response, its weak-anisotropy coefficient, and a strict one-contact approximation gap. Finite-dictionary analysis connects these formulas to non-negative synthesis. The contribution is a quantitative specialization of established geometric constructions, with the lollipop problem supplying a concrete target.

2 The WGS84 target and its spectral content

Write $f = (a_E - b_E)/a_E$ for ellipsoidal flattening. WGS84 specifies $f^{-1} = 298.257223563$ [1]. Rescale the equatorial semiaxis to R_0 and use colatitude θ. The spheroid's exact radial coordinate is

$$r_f(\theta) = R_0 \left(\sin^2\theta + \frac{\cos^2\theta}{(1-f)^2} \right)^{-1/2}. \tag{2}$$

Taylor expansion, uniform in θ, gives

$$R_0 - r_f(\theta) = R_0 f \cos^2\theta + O(R_0 f^2), \qquad \delta_\star(\theta) := R_0 f \cos^2\theta. \tag{3}$$

Proposition 2.1. *In real orthonormal spherical harmonics, the first-order target is*

$$\delta_\star = R_0 f \left(\frac{\sqrt{4\pi}}{3} Y_0^0 + \frac{2}{3}\sqrt{\frac{4\pi}{5}} Y_2^0 \right). \tag{4}$$

Its integral is $4\pi R_0 f/3$, and its squared L^2 norm is $4\pi (R_0 f)^2/5$.

Proof. Use $t^2 = (1 + 2P_2(t))/3$, $Y_0^0 = (4\pi)^{-1/2}$, and $Y_2^0 = \sqrt{5/(4\pi)}P_2(\cos\theta)$. The integrals follow from $\int_{\mathbb{S}^2} g(\cos\theta)\,\mathrm{d}A = 2\pi\int_{-1}^{1} g(t)\,\mathrm{d}t$. □

The first-order removed volume is $4\pi R_0^3 f/3$, consistent with the sphere–spheroid volume difference. At second order the radial removal includes $(3R_0 f^2/2)(\cos^2\theta - \cos^4\theta)$, introducing degree four. Spectral sparsity is therefore exact for the linearized target only. Localized actuators fitted to it generally excite higher degrees.

3 Frames, kernels, and physical orientation

For $x \in \mathbb{S}^2$, choose unit orthogonal tangent vectors e_1, e_2 with $e_1 \times e_2 = x$. Then $R = [e_1\ e_2\ x] \in \mathrm{SO}(3)$. This identifies the oriented orthonormal frame bundle with $\mathrm{SO}(3)$. Right multiplication by $Q_\psi = \mathrm{diag}(q_\psi, 1)$, with q_ψ a planar rotation, preserves x and rotates the tangent frame. Its base is $\mathbb{S}^2 \cong \mathrm{SO}(3)/\mathrm{SO}(2)$ [7].

Fix $0 < r_c < \pi$. Let χ be non-negative and smooth, positive for $0 \le r < r_c$, zero for $r \ge r_c$, and a smooth function of r^2 near zero. For $d(x,y) < r_c$, define

$$u_R(y) = \begin{pmatrix} \langle \mathrm{Log}_x\, y, e_1 \rangle \\ \langle \mathrm{Log}_x\, y, e_2 \rangle \end{pmatrix}. \tag{5}$$

For $a > |b|$ set $\Lambda = \mathrm{diag}(a+b, a-b)$ and

$$K_{a,b}(y; R) = Z_{a,b}^{-1} \chi(r) \exp\!\left(-\tfrac{1}{2} u_R(y)^\top \Lambda u_R(y) \right), \qquad r = d(x,y), \tag{6}$$

with value zero outside the cap. The cutoff avoids the antipodal cut locus; $Z_{a,b} > 0$ makes $\int K_{a,b}\,\mathrm{d}A = 1$. Logarithmic coordinates have angular length units on the unit sphere.

Proposition 3.1. *The normalization is independent of R, and the kernels are equivariant under ambient rotations. For $b = 0$ the kernel depends only on the centre. For $b \neq 0$ its fibre stabilizer is exactly $\psi \in \pi\mathbb{Z}$.*

Proof. Ambient rotations preserve distance, area, and the exponential map. Under $R \mapsto RQ_\psi$, coordinates change to $q_\psi^\top u_R$. For $b = 0$ the quadratic form is radial. Otherwise equality on a neighbourhood of the centre requires $q_\psi \Lambda q_\psi^\top = \Lambda$. Since the eigenvalues are distinct, a planar rotation satisfies this exactly at 0 or π modulo 2π. □

An elliptical footprint records an unoriented axis. For fixed nonzero b its minimal state can be represented by $\mathrm{SO}(3)/\{I, Q_\pi\}$; a full frame retains a two-fold redundancy. We use SO(3) because transport acts naturally on frames. If covariance is also variable, rotating the basis and transforming its coordinate matrix simultaneously is merely a coordinate change. Here the precision matrix is fixed in the transported frame, so a fibre rotation changes the physical footprint.

4 An exact orientation-response formula

Write $u_R = r(\cos\phi, \sin\phi)^\top$. The area element is $\sin r \,\mathrm{d}r\,\mathrm{d}\phi$ and

$$K_{a,b}(r, \phi; R) = Z_{a,b}^{-1} \chi(r) e^{-ar^2/2} e^{-br^2 \cos(2\phi)/2}. \tag{7}$$

We use the modified Bessel integral $I_0(t) = (2\pi)^{-1} \int_0^{2\pi} e^{t\cos u}\,\mathrm{d}u$ [8]; I_0 is even.

Theorem 4.1 (Kernel overlap)**.** *For $K = K_{a,b}(\cdot; R)$ and $K_\psi = K_{a,b}(\cdot; RQ_\psi)$,*

$$Z_{a,b} = 2\pi \int_0^{r_c} \chi(r) e^{-ar^2/2} I_0(br^2/2) \sin r \,\mathrm{d}r, \tag{8}$$

$$C(\psi) := \langle K, K_\psi \rangle = \frac{2\pi}{Z_{a,b}^2} \int_0^{r_c} \chi(r)^2 e^{-ar^2} I_0(br^2 \cos\psi) \sin r \,\mathrm{d}r. \tag{9}$$

The squared mismatch $D_\psi^2 := \|K - K_\psi\|_2^2$ is

$$D_\psi^2 = \frac{4\pi}{Z_{a,b}^2} \int_0^{r_c} \chi(r)^2 e^{-ar^2} [I_0(br^2) - I_0(br^2\cos\psi)] \sin r \,\mathrm{d}r. \tag{10}$$

For $b \neq 0$ it vanishes exactly at $\psi \in \pi\mathbb{Z}$ and is maximal at $\psi \in \pi/2 + \pi\mathbb{Z}$.

Proof. Angular integration of (7) gives (8). In the product, use

$$\cos(2\phi) + \cos(2\phi - 2\psi) = 2\cos\psi \cos(2\phi - \psi).$$

The angular integral is $2\pi I_0(br^2\cos\psi)$, proving (9). Rotation invariance implies $\|K\|_2^2 = \|K_\psi\|_2^2 = C(0)$, hence $D_\psi^2 = 2[C(0) - C(\psi)]$. The series $I_0(t) = \sum_{k=0}^\infty (t^2/4)^k/(k!)^2$ is strictly increasing in $|t| > 0$. Positivity of χ gives the claimed zero set and maxima. □

Corollary 4.2 (Weak anisotropy)**.** *For fixed a, χ, ψ, as $b \to 0$,*

$$D_\psi^2 = \frac{\pi b^2 \sin^2\psi}{Z_{a,0}^2} \int_0^{r_c} \chi(r)^2 e^{-ar^2} r^4 \sin r \,\mathrm{d}r + O(b^4). \tag{11}$$

For $\sin\psi \neq 0$, $D_\psi = c_a |b \sin\psi| + O(|b|^3)$, where

$$c_a = Z_{a,0}^{-1} \sqrt{\pi \int_0^{r_c} \chi(r)^2 e^{-ar^2} r^4 \sin r \,\mathrm{d}r} > 0.$$

At a symmetry angle the mismatch is identically zero.

Proof. The expansion $I_0(t) = 1 + t^2/4 + O(t^4)$ is uniform on the compact radial interval. The bracket in (10) is $b^2 r^4 \sin^2 \psi/4 + O(b^4)$, while $Z_{a,b} = Z_{a,0} + O(b^2)$. Substitution and, when the leading coefficient is positive, taking a square root complete the proof. ☐

Corollary 4.3 (One-contact approximation gap)**.** *If the target is K and the only available atom is K_ψ, then*

$$\alpha_\star = \frac{C(\psi)}{C(0)}, \qquad \min_{\alpha \geq 0} \|K - \alpha K_\psi\|_2^2 = C(0) - \frac{C(\psi)^2}{C(0)}. \tag{12}$$

For $b \neq 0$ and $\psi \notin \pi\mathbb{Z}$, the residual is strictly positive. Admitting the target frame gives zero residual with one contact.

Proof. Minimize the quadratic in α. The overlap is positive, so its unconstrained minimizer is feasible. Cauchy–Schwarz is strict unless the kernels are proportional; their equal integrals then force equality, excluded by Proposition 3.1. ☐

This comparison uses the same anisotropic actuator at different orientations. It does not imply a universal advantage over isotropic kernels of independently chosen width or over arbitrary multi-contact schemes.

5 Holonomy and transport-constrained actuation

A tangent vector along a smooth path $x(s) \in \mathbb{S}^2$ is parallel transported when

$$\dot{v} = -(v \cdot \dot{x})x. \tag{13}$$

Its tangential derivative is zero. Direct differentiation also shows preservation of $v \cdot x = 0$ and $\|v\|^2$. Transporting both tangent columns preserves a frame.

Proposition 5.1 (Holonomy response)**.** *Let two paths share an initial frame and the same terminal point. Suppose their concatenation, the first followed by the reverse of the second, is a simple oriented loop enclosing area A_Ω. The terminal frames differ by $\psi = \pm A_\Omega$ modulo 2π, and their terminal kernels have mismatch D_{A_Ω} from (10). For $b \neq 0$ it vanishes exactly at $A_\Omega \in \pi\mathbb{Z}$.*

Proof. The holonomy form of Gauss–Bonnet gives $\int_\Omega K_G \, \mathrm{d}A$ modulo 2π for the Levi-Civita connection [9]. On the unit sphere $K_G = 1$. The sign depends on comparison order and is immaterial because (10) is even in ψ. ☐

A latitude of colatitude θ_0 bounds the northern cap, giving

$$\psi = 2\pi(1 - \cos\theta_0) \pmod{2\pi}. \tag{14}$$

At $\theta_0 = \pi/4$ this is 1.840302369021 radians. At $\theta_0 = \pi/3$ it is π: both tangent axes reverse, but the ellipse is unchanged. This is nontrivial frame holonomy with zero actuation response. At the equator the cap area is 2π, equivalent to zero frame rotation.

The sum (1) is commutative when the summands are fixed. History enters through $R_j = \mathcal{P}_{\gamma_j} R_{j-1}$, where $\mathcal{P}$ denotes transport along a prescribed travel segment. Changing a route can change R_j and hence the summands. Independent orientation resets remove this history effect. Equations (10) and (14) quantify it under the no-reset assumption.

6 Finite non-negative synthesis

Fix unit-integral non-negative kernels $K_1, \dots, K_M$, a target $d \in L^2(\mathbb{S}^2)$, and $\lambda \geq 0$. Consider

$$J(\alpha) = \left\| d - \sum_{j=1}^{M} \alpha_j K_j \right\|_2^2 + \lambda \sum_{j=1}^{M} \alpha_j, \qquad \alpha \geq 0. \tag{15}$$

The regularizer penalizes total integrated removal. It is the ℓ^1 norm of the coefficients, but does not guarantee a minimum number of contacts.

Proposition 6.1. *A minimizer of (15) exists, and all minimizers give the same fitted field. Linear independence of the dictionary implies unique coefficients. Enlarging the dictionary cannot increase the minimum objective.*

Proof. For $s = \sum_j \alpha_j K_j \geq 0$, normalization and Cauchy–Schwarz give

$$\|\alpha\|_1 = \int_{\mathbb{S}^2} s \, \mathrm{d}A \leq \sqrt{4\pi}\, \|s\|_2 \leq \sqrt{4\pi}(\|s - d\|_2 + \|d\|_2).$$

Every sublevel set of J is therefore bounded in the closed orthant; continuity gives existence. If two minimizers had different fitted fields, the midpoint would strictly reduce the squared residual while preserving the mean linear penalty, a contradiction. Linear independence makes the coefficient-to-field map injective. Appending zero coefficients embeds every old solution in an enlarged dictionary. □

For positive quadrature weights w_i and $B_{ij} = K_j(y_i)$, replace the norm by $\sum_i w_i(d_i - (B\alpha)_i)^2$. Existence follows similarly when every column has positive weighted mass. Convexity makes the following optimality conditions necessary and sufficient:

$$g = 2B^\top W(B\alpha - d) + \lambda \mathbf{1} \geq 0, \quad \alpha \geq 0, \quad \alpha_j g_j = 0. \tag{16}$$

This is a convex problem for strengths at fixed frames. Optimizing centres or transport routes is a separate, generally nonconvex problem.

7 Numerical validation

Three reproducible tests check transport convergence, independent integration of the orientation response, and finite non-negative fitting.

7.1 Parallel transport

Classical fourth-order Runge–Kutta integrates (13) along $x(\phi) = (\sin\theta_0 \cos\phi, \sin\theta_0 \sin\phi, \cos\theta_0)$ from $v(0) = (\cos\theta_0, 0, -\sin\theta_0)$. The terminal vector is projected onto the initial tangent plane and normalized before measuring its angle. Table 1 gives step refinement at $\theta_0 = \pi/4$. At 20,000 steps the result is 1.840302369020 rad, with wrapped error 8.0×10^{-13} rad. This is near the floating-point floor and is not used to estimate convergence order.

7.2 Kernel mismatch and weak anisotropy

Use the smooth cutoff

$$\chi(r) = \begin{cases} \exp[-r^2/(r_c^2 - r^2)], & 0 \leq r < r_c, \\ 0, & r \geq r_c, \end{cases} \qquad r_c = 1.2. \tag{17}$$

Steps	Wrapped error (rad)	Ratio	Order
64	$1.432e-07$	–	–
128	$8.884e-09$	16.120	4.011
256	$5.529e-10$	16.067	4.006
512	$3.447e-11$	16.042	4.004
1024	$2.218e-12$	15.542	3.958

Table 1: Latitude-loop error at $\theta_0 = \pi/4$. Ratio compares successive errors; order is its base-two logarithm.

Set $a = 16$, $b = a\epsilon$, and $\psi = 2\pi(1-1/\sqrt{2})$. The covariance eigenvalue ratio is $(1+|\epsilon|)/(1-|\epsilon|)$; ϵ is a precision contrast. Evaluate (9) with 256-point radial Gauss–Legendre quadrature. Independently integrate $(K - K_\psi)^2$ with 160 radial and 256 equispaced angular nodes, then refine to 320 and 512 nodes. Each direct kernel is normalized by its own two-dimensional integral. The script requires absolute discrepancies below 2×10^{-10} for both comparisons and checks isotropic and half-turn symmetries. The logarithmic slope from $\epsilon = 0.01$ to 0.02

$\epsilon = b/a$	$D_\psi/\|K\|_2$	D_ψ
0.00	0.000000	0.000000
0.01	0.008618	0.010409
0.02	0.017236	0.020817
0.05	0.043101	0.052036
0.10	0.086272	0.104024
0.20	0.173114	0.207656
0.40	0.350946	0.412036
0.60	0.539096	0.609242

Table 2: Response to the $\pi/4$ latitude holonomy. Relative mismatch is $D_\psi/\|K\|_2$.

is checked against one, as predicted by Corollary 4.2. The mismatch norm is first order; its square is second order. The measured slope is 0.999973 and the predicted coefficient in $D_\psi = 1.040885\,|\epsilon| + O(|\epsilon|^3)$ agrees with the small-contrast calculation. The largest absolute discrepancy between the direct and Bessel evaluations in Table 2 is below 1.3×10^{-14}.

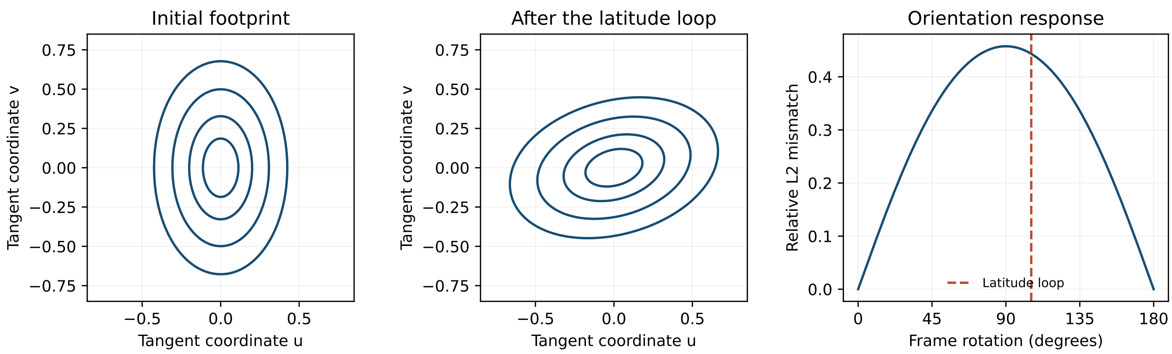

Figure 1: The kernel with $a = 16$, $b = 8$ before and after transport around the $\pi/4$ latitude, shown in logarithmic tangent coordinates. Contours are at 10, 30, 60, and 85 percent of peak height. The response curve returns to zero at a half-turn, reflecting the symmetry of an elliptical footprint.

7.3 A nested-orientation benchmark

Divide the first-order WGS84 target by $R_0 f$, obtaining $d(y) = y_3^2$. Take $a = 8$, $b = 4$, $r_c = 1.2$, and $\lambda = 0$. Use twelve fixed centres, indexed by $j = 0, \ldots, 11$:

$$z_j = 1 - 2(j + 1/2)/12, \qquad \phi_j = j\pi(3 - \sqrt{5}), \tag{18}$$

$$x_j = (\sqrt{1 - z_j^2}\cos\phi_j, \sqrt{1 - z_j^2}\sin\phi_j, z_j). \tag{19}$$

Choose $e_1 = ((0,0,1) \times x_j)/\|(0,0,1) \times x_j\|$ and $e_2 = x_j \times e_1$. Compare the twelve-atom dictionary with fibre angle zero to the forty-eight-atom dictionary with angles $0, \pi/4, \pi/2, 3\pi/4$ at every centre. Both use the same anisotropic footprint, and the first is a subset of the second.

Non-negative least squares uses 48 Gauss–Legendre nodes in z and 96 equispaced longitudes. Hold the fitted strengths fixed and validate on a 96-by-192 grid. Table 3 reports relative L^2 errors. Active coefficients exceed 10^{-9}. With $h = B^\top W(B\alpha - d)$, the reported KKT residual is $\max\{\|(-h)_+\|_\infty, \|\alpha \odot h\|_\infty\}$. This illustrates feasible-set inclusion. The number of candidate atoms changes, so the comparison does not isolate orientation from dictionary size or show an equal-budget advantage. Nor does it establish global optimality over centres, contact count, width, or routes.

Atoms	Active	Fit error	Validation error	KKT residual
12	12	0.471593	0.471593	$3.44e-16$
48	20	0.436528	0.436528	$2.64e-16$

Table 3: Approximation of $d(y) = y_3^2$. Orientations are freely selected; these are not transport-constrained route optimizations.

8 Discussion

The lollipop target is spectrally sparse at first order, while an anisotropic actuator retains a tangent axis. The overlap formula makes this axis dependence quantitative. A nonzero holonomy need not change the footprint: a half-turn is an elliptical symmetry. Weak-anisotropy mismatch is linear in precision contrast and proportional, at leading order, to $|\sin\psi|$.

The model uses a fixed sphere, compact logarithmic Gaussian kernels, and non-negative additive removal. No-twist transport is a prescribed control constraint; a real tool may rotate actively or slip. An evolving surface would change its metric, normalization, and transport law. Continuous removal during travel requires a path integral of footprints. Finite-dictionary fitting does not solve that control problem. Optimizing travel sequences with both removal error and travel cost is a natural extension.

Data and code

Source, scripts, generated tables, and machine-readable results are available in the GitHub source directory. All data are synthetic. Numerical settings, tolerances, and library versions are recorded with the results.

Acknowledgements

No dedicated funding or competing interests are reported. No human or animal subjects or personal datasets were used.

References

[1] National Geospatial-Intelligence Agency, *World Geodetic System 1984*, defining parameters, https://earth-info.nga.mil/index.php?dir=wgs84&action=wgs84.

[2] J.-P. Antoine, L. Demanet, L. Jacques, and P. Vandergheynst, Wavelets on the sphere: implementation and approximations, *Applied and Computational Harmonic Analysis* **13**(3), 177–200 (2002). doi:10.1016/S1063-5203(02)00507-9.

[3] T. Cohen, M. Weiler, B. Kicanaoglu, and M. Welling, Gauge Equivariant Convolutional Networks and the Icosahedral CNN, *Proceedings of Machine Learning Research* **97**, 1321–1330 (2019). https://proceedings.mlr.press/v97/cohen19d.html.

[4] S. C. Schonsheck, B. Dong, and R. Lai, Parallel Transport Convolution: Deformable Convolutional Networks on Manifold-Structured Data, *SIAM Journal on Imaging Sciences* **15**(1), 367–386 (2022). doi:10.1137/21M1407616.

[5] R. A. Jones, Optimization of computer controlled polishing, *Applied Optics* **16**(1), 218–224 (1977). doi:10.1364/AO.16.000218.

[6] H.-Y. Tam and H. Cheng, An investigation of the effects of the tool path on the removal of material in polishing, *Journal of Materials Processing Technology* **210**(5), 807–818 (2010). doi:10.1016/j.jmatprotec.2010.01.012.

[7] J. M. Lee, *Introduction to Riemannian Manifolds*, 2nd ed., Springer (2018). doi:10.1007/978-3-319-91755-9.

[8] NIST Digital Library of Mathematical Functions, §10.32, Integral Representations of Modified Bessel Functions, https://dlmf.nist.gov/10.32.

[9] M. P. do Carmo, *Riemannian Geometry*, Birkhäuser (1992). doi:10.1007/978-1-4757-2201-7.